



# Effect of Processing Conditions on Short-Range Order and Mechanical Properties of the NbMoTaW Multi-Principal Element Alloy

Hui Zheng<sup>1</sup> · Luke Nibbelink<sup>2</sup> · Xiang-Guo Li<sup>1</sup> · Yunxing Zuo<sup>1</sup> · Chi Chen<sup>1</sup> · Shyue Ping Ong<sup>1</sup>

Received: 6 June 2024 / Accepted: 1 July 2025  
© The Author(s) 2025

## Abstract

Refractory multi-principal element alloys (RMPEAs) are promising candidates for high-temperature applications due to their exceptional mechanical properties. In this work, we investigate the effect of processing conditions on the observed short-range order (SRO) in the NbMoTaW RMPEA, and the consequent effect on mechanical properties, using Monte Carlo/molecular dynamics (MC/MD) simulations with a highly accurate machine learning interatomic potential. We demonstrate that SRO is maximized at an intermediate temperature range of 800K–1000K. A higher SRO results in higher stacking fault energies (SFEs), anti-phase boundary energies (APBEs), and critical resolved shear stresses (CRSS). We also show that Nb segregation in polycrystalline NbTaMoW is also present at intermediate annealing temperatures, and this Nb segregation can have the effect of retarding grain growth even at high temperatures.

## Introduction

Multi-principal element alloys (MPEAs) comprise multiple metals in near-equiatomic proportions. [1–3]. In recent years, refractory MPEAs (RMPEAs) have garnered immense interest because of their exceptional mechanical properties at high temperatures. For instance, the NbTaMoW RMPEA has been shown to exhibit high strength at temperatures exceeding 1800K, making them potential candidates for aerospace and other applications.

While MPEAs were initially conceived of as random solid solutions (RSS), recent experimental and computational evidence suggest that MPEAs can exhibit chemical short-range ordering (SRO), particularly at lower temperatures [4–8]. This SRO can, in turn, have an effect on mechanical properties. For instance, Ding et al. reported a positive correlation between the degree of SRO and the stacking fault energy in the fcc NiCoCr MPEA [9]. Experimentally, Zhang et al. [4] also found that the increasing amounts of SRO give rise

to both higher SFEs and hardness. On the other hand, Yin et al. [10] reported that SRO has a negligible influence on alloy strength and hardness for samples annealed at 600 and 700°C (i.e., 873 and 973K).

Previously, the present authors have developed highly accurate machine learning interatomic potentials (ML-IAPs) for the NbTaMoW RMPEA based on the spectral neighbor analysis potential (SNAP) [8] and moment tensor potential (MTP) formalisms. [11] ML-IAPs, which parameterize the potential energy surface as a function of local environment descriptors using machine learning, are a modern alternative to classical IAPs. [12] While somewhat more computationally expensive, ML-IAPs offer substantially improved accuracy and flexibility, especially for complex systems such as MPEAs. [8, 13–17] By performing atomistic simulations with a NbTaMoW SNAP, we previously demonstrated that Nb tends to preferentially segregate to the grain boundaries of the NbTaMoW polycrystal, which enhances the observed bulk SRO and leads to increased strength. [8] We have also shown that SRO enhances the mobility of edge dislocations but decreases the rate of double-kink nucleation in the motion of screw dislocations [11].

One of the key simplifying assumptions in our previous work is that the observed SRO at a given temperature is based on thermodynamic equilibrium within Monte Carlo/molecular dynamics (MC/MD) simulations. However, kinetic barriers for atomic migration can lead to the stabilization of non-equilibrium atomic arrangements. Synthesis

✉ Shyue Ping Ong  
ongsp@eng.ucsd.edu

<sup>1</sup> Department of NanoEngineering, University of California San Diego, 9500 Gilman Dr, Mail Code 0448, La Jolla, CA 92093-0448, United States

<sup>2</sup> Materials Science and Engineering, University of California San Diego, 9500 Gilman Dr, Mail Code 0448, La Jolla, CA 92093-0448, United States

of RMPEAs is usually carried out at extremely high temperatures ( $> 2000\text{K}$ ), followed by quenching and annealing at lower temperatures. The initial high-temperature RMPEA structure would resemble a RSS, but the eventual SRO within the RMPEA depends on the annealing temperature and time.

In this work, we explore the effect of annealing temperature and time on observed SRO in the NbTaMoW RMPEA using our previously developed SNAP for this system. We also provide a statistical analysis of the effect of SRO on the distribution of key mechanical properties such as stacking fault energies (SFEs), anti-phase boundary energies (APBEs), and critically resolved shear stresses (CRSSs).

## Methods

### Nudged Elastic Band (NEB) calculations

Density functional theory (DFT) nudged elastic band (NEB) calculations of the vacancy migration barriers were performed using the Vienna Ab initio Simulation Package (VASP) [18] within the projector augmented-wave approach [19]. The Perdew–Burke–Ernzerhof (PBE) generalized-gradient approximation (GGA) functional [20] was used for all the relaxations. All input generation and analysis were performed using the pymatgen-analysis-diffusion [21, 22] package. A  $3 \times 3 \times 3$  supercell relative to the bcc conventional unit cell was used to sample 20 different configurations of the RMPEA for each migrating element.

From Fick's law, the diffusion length of a species  $x$  is related to the migration barrier, temperature, and time by the following relation [23]:

$$x \propto \sqrt{D_0 \cdot \exp\left(\frac{-E_a}{k_B T}\right) \cdot t}, \quad (1)$$

where  $D_0$  is a temperature-independent pre-exponential factor,  $E_a$  is the activation energy,  $k_B$  is the Boltzmann constant,  $T$  is the temperature, and  $t$  is the time. In this work, a  $D_0$  value of  $0.1 \text{ m}^2\text{s}^{-1}$  is selected based on the experimental value for Nb diffusion in Mo [24]. The maximum value  $D_0 = 0.02 \text{ m}^2\text{s}^{-1}$  is selected from experimental values of W self-diffusion as shown in Table 1 [24].

### Atomistic Simulations

All atomistic simulations were performed using the LAMMPS code [25], and analysis of the atomic structures was performed using the OVITO software [26]. The ML-IAP used is the NbTaMoW SNAP previously developed by some of the current authors, and interested readers are

**Table 1** The mean values of  $E_{KRAB}^m$  and experimentally reported  $D_0$

Migration element	Mean values of $E_{KRAB}^m$	Reported $D_0$ ( $\times 10^{-4} \text{ m}^2\text{s}^{-1}$ ) [24]
Nb	1.05	0.61, 1.1, 3.7, 4.6, 65 (Self-diffusion) 1000 (Nb diffusion in Mo)
Ta	1.13	0.09, 0.21, 1, 1.16 (Self-diffusion)
Mo	1.44	0.13, 2.77, 5.7, 8, 139 (Self-diffusion)
W	1.50	0.13, 1.88, 15.3, 46, 200 (Self-diffusion)

directed to ref 8 for details of its formalism, development, and performance metrics.

Hybrid MC/MD simulations under isobaric–isothermal (NPT) ensemble were conducted to obtain the equilibrium configurations at different annealing temperatures  $T_a$ . The initial RMPEA bulk structure was initialized with a random arrangement of NbMoTaW in equiatomic proportions. The bcc supercell contains 3456 atoms with cube edges of  $\sim 39 \text{ \AA}$ . The MD time step was set to 2 fs. A Nose–Hoover thermostat was used to control the temperature. For every MD step, there is one MC cycle. A total of 1,000,000 steps were carried out at each  $T_a$ . The converged configurations were then equilibrated at 300 K for 30 ps within an NPT ensemble, followed by structure relaxation at 0 K for subsequent property calculations, e.g., stacking fault energies (SFEs), APBE, etc.

### Stacking Fault Energy Calculations

For the SFE and APBE calculations, the equilibrated structures were re-oriented with the  $x$ ,  $y$ , and  $z$  directions along the  $[112]$ ,  $[\bar{1}10]$ , and  $[11\bar{1}]$  cube directions, respectively. A  $12 \times 12 \times 12$  supercell size (20,736 atoms) is used to calculate SFE and APBE based on the oriented structure. The conjugate gradient algorithm (CG) was used to perform stacking fault structure relaxations and energy minimizations. The force components within the stacking fault plane were set to zero, and the direction perpendicular to the fault plane was allowed to relax. Supplementary Information Figures S2 (a) and (c) show the atomic structures of the stacking fault on  $(1\bar{1}\bar{1})$  plane and  $(112)$  plane, respectively. The unstable SFEs are the maximum values of the SFE pathway in Supplementary Information Figure S2 (b) and (d), which correspond to a shift of half of the Burgers vector. The APBEs are the local minimum values of the SFE path in Supplementary Information Figure S2 (b) and (d), which correspond to a shift of one Burgers vector. We sampled stacking faults by changing the cutting layer positions along  $[\bar{1}10]$  or  $[112]$  direction and shifting one half along with  $[11\bar{1}]$  direction relative to the other half over 24 Burgers vectors [13].

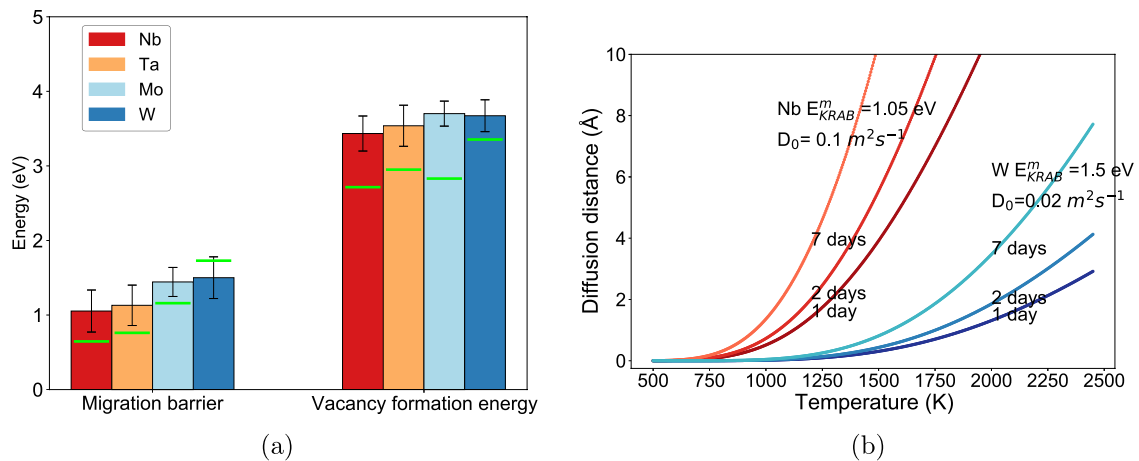


**Fig. 1** **a** Vacancy formation energy ( $E_f^v$ ) and the kinetically resolved activation barriers of migration ( $E_{KRAB}^m$ ) for Nb, Ta, Mo, and W in RMPEA. The error bars represent the standard deviations from 20 sampled RSS MPEAs for migration barrier and 40 sampled RSS MPEAs for vacancy formation energy. The vacancy formation energy is calculated using the equation  $E_f^v = E_v - E_0 + \mu_{el}$ , where  $E_v$  and  $E_0$  are the energies of the supercell with and without a vacancy, respectively.  $\mu_{el}$  represents the chemical potential of the removed element, taken as the energy per atom of the corresponding pure metal in its

ground state bulk form at 0K. The migration barrier is calculated as the energy difference between the intermediate image and the initial state using the `pymatgen.analysis.transition_state` class. The green line segments are the corresponding  $E_f^v$  and  $E_{KRAB}^m$  in the pure elemental metals from ref 36. **b** plots showing the contours of the estimated diffusion distance ( $x$ ) as a function of time and annealing temperature based on the mean migration barrier of 1.5 eV (bluish lines) for W and the mean migration barrier of 1.05 eV (red-dish lines) for Nb based on Equation 1 (Color figure online)

## Critical Resolved Shear Stress (CRSS) of Screw Dislocation

A  $1/2 \langle 111 \rangle$  screw dislocation line was inserted in the oriented structures ( $x$ -[112],  $y$ -[110],  $z$ -[111]) [27, 28] for the equilibrated structures annealed at 800K, 1000K, and 1200K. A cylinder with a radius of 47 Å was carved from the oriented supercell, which is generated by doubling the size along  $y$  direction of the structure used for SFE/APBE calculations with the lattice length  $\sim 95 \text{ Å} \times 110 \text{ Å} \times 67 \text{ Å}$ . The cylinder has 27,475 atoms, as shown in Supplementary Information Figure S3. An inner cylinder with a radius of 42 Å and an axis along  $z$ -direction was selected to be the mobile region during the loading process. The outside shell was treated as a rigid body. A periodic boundary condition was imposed along the  $z$ -direction, and shrink-wrapped non-periodic boundary conditions were imposed in  $x$ - and  $y$ -directions.

The atoms of the outer shell were moved along  $z$ -direction at a velocity  $v_z$  that is a function of  $y$  atom coordinates as given below [29]:

$$v_z = 0.001 \times (y - l_y/2), \quad (2)$$

where  $l_y$  is the box length. In effect, shear stress is applied along the  $z$ -direction, resulting in a movement of the screw dislocation core along the  $x$  direction. The stress at the start of the movement is the critical resolved shear stress (CRSS).

## Tensile Load Simulations

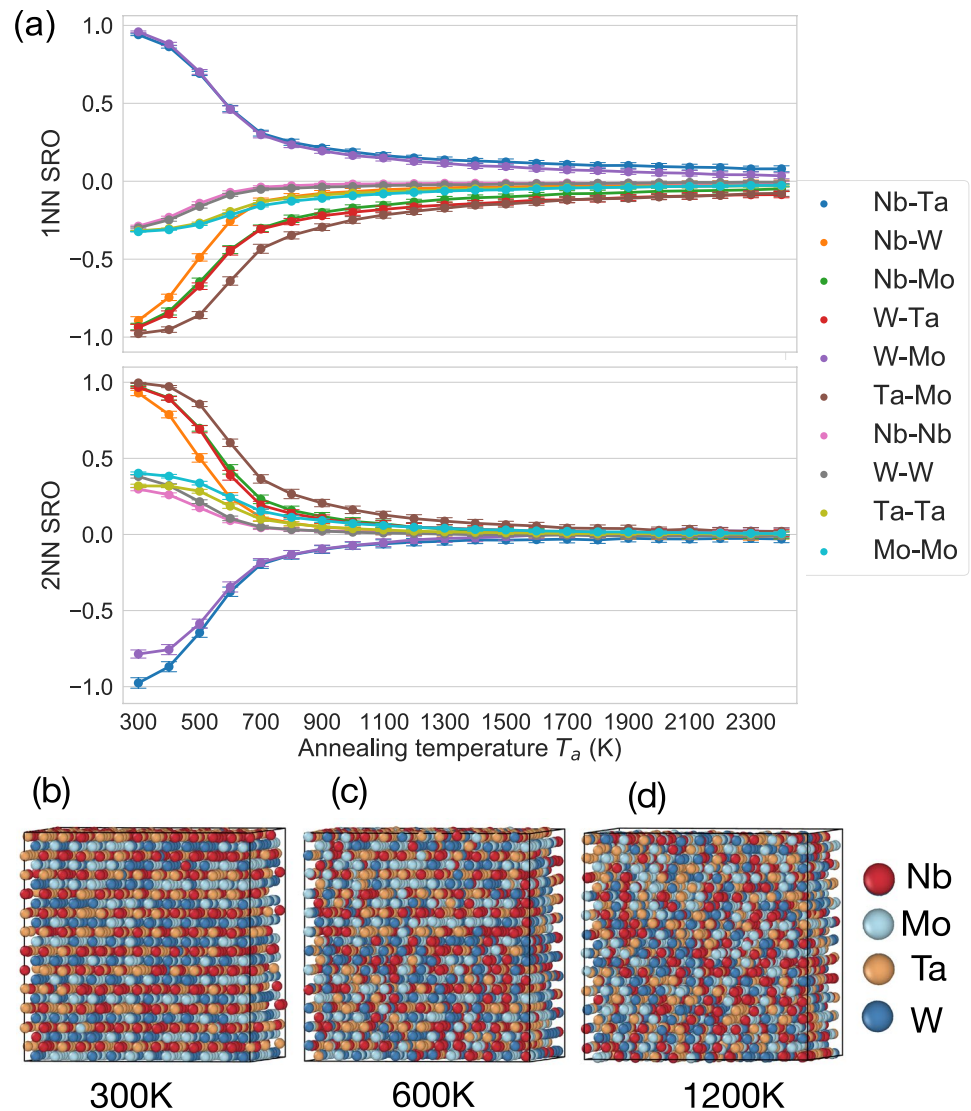
For tensile load simulations, the structures annealed from MC/MD calculations at various temperatures were equilibrated under an NPT ensemble at zero pressure and 300K for 50 ps. Tensile loading was applied by expanding the simulation box size along  $z$ -<001> direction at a strain rate of  $5 \times 10^8 \text{ s}^{-1}$  and a time step of 1 fs. Two sizes of the bulk cells were used for the strain–stress simulation. For the temperature-dependent strain–stress curves in Figure 4, the same cell size obtained from MC/MD calculations was used. To investigate the complex mechanisms under tension,  $3 \times 3 \times 3$  supercells of the equilibrated MC/MD cells with were generated. The supercell has dimensions  $\sim 114 \text{ Å} \times 114 \text{ Å} \times 114 \text{ Å}$  and a total of 93,312 atoms.

## Chemical SRO Parameters

The Warren–Cowley pairwise SRO parameter [8, 30]  $\alpha_{ij}^k$  quantifies the chemical order around a central atomic species  $i$  with other species  $j$  within the  $k$ -th nearest-neighbor shells and is defined as follows:

$$\alpha_{ij}^k = \frac{p_{ij}^k - c_j}{\delta_{ij} - c_j}, \quad (3)$$

**Fig. 2** Short-range order (SRO) of bulk MPEA from different annealing temperatures  $T_a$ . **a** Pairwise SRO of bulk MPEA annealed from different temperatures from 300 K to 2400 K. The error bars reflect the standard deviation of the SROs of the last 100 snapshot structures collected from each MC/MD simulation at intervals of 2 ps. **b–d** Atomic structure representatives after 2 ns MC/MD calculations at  $T_a = 300$ , 600, and 1200 K, respectively. Elements belonging to the same group are colored with similar colors (red: Nb, orange: Ta; light blue: Mo, blue: W) (Color figure online)



where  $p_{ij}^k$  denotes the average probability of finding a  $j$ -type atom around an  $i$ -type atom in the  $k$ -th shell,  $c_j$  is the average concentration of  $j$ -type atom in the system, and  $\delta_{ij}$  is the Kronecker delta function. For  $i = j$ , a positive (negative)  $\alpha_{ij}^k$  implies the tendency for pairs of the same species in the  $k$ -th shell to attract (repel) each other. For  $i \neq j$ , a positive (negative)  $\alpha_{ij}^k$  implies the tendency for pairs of species  $i$  and  $j$  in the  $k$ -th shell to repel (attract) each other, i.e., opposite in sign from  $i = j$ .

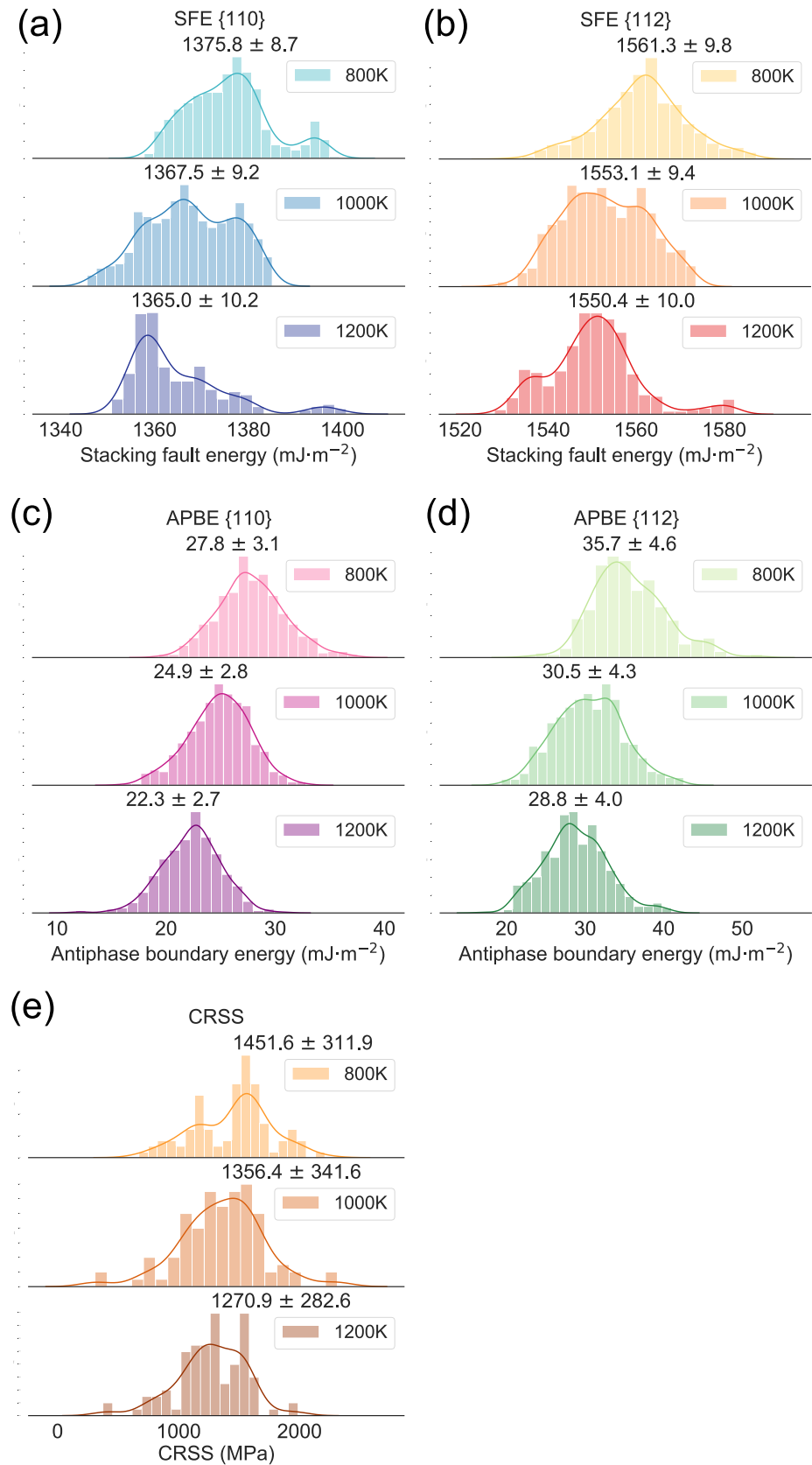
## Results and Discussion

### Vacancy Migration Barriers in NbTaMoW

Figure 1a shows the calculated vacancy formation energies ( $E_f^v$ ) and kinetically resolved migration barriers ( $E_{KRAB}^m$ ) [31]

for the different elements in the random solid solution (RSS) NbTaMoW RMPEA. The error bars in the bar plot represent the standard deviations across different local chemical environments, derived from 20 RSS samples for migration barriers and 40 RSS samples for vacancy formation energies. Both properties follow similar elemental ordering: Nb < Ta < Mo  $\approx$  W. Notably, vacancy formation energies in the RMPEA are consistently higher than in their pure metal counterparts (indicated by green lines), suggesting increased lattice stability in the multi-component system. This enhancement can be attributed to the complex local chemical environments and lattice distortions characteristic of high-entropy alloys. A similar trend is observed when the vacancy formation energy ( $E_f^v$ ) is calculated using the SNAP potential, as shown in Supplementary Information Figure S1. Migration barriers also exhibit element-specific behavior, with Nb showing the lowest barrier and W the highest. This

**Fig. 3** **a** and **b** are the distributions of SFE of faults on {110} and {112} planes, respectively. **c** and **d** are the distributions of anti-phase boundary energy on {110} and {112} planes, respectively. **e** is the distribution of CRSS from various SROs obtained from  $T_d = 800, 1000,$  and  $1200$  K





suggests that Nb vacancies would demonstrate the highest mobility in this system at finite temperatures, potentially influencing diffusion-mediated processes such as the formation of short-range order and segregation. The statistical variation across different atomic configurations (represented by error bars) indicates that local chemical environments significantly impact both properties, highlighting the importance of comprehensive sampling in accurately modeling these complex alloy systems.

Experimentally, the NbTaMoW RMPEA is typically synthesized by arc melting from the pure metals and homogenized at 1800 K [32, 33]. This temperature is sufficiently high that a relatively high concentration of vacancies ( $\sim 10^{-4} - 10^{-6}$  [34, 35]) should be formed during the initial synthesis. Figure 1b plots contours of the estimated diffusion distance as a function of time and annealing temperature (Equation 1) based on the lowest and highest average  $E_{KRAB}^m$  of 1.05 eV and 1.5 eV for Nb and W, respectively, in the MPEA. We may conclude that negligible vacancy diffusion is expected at temperatures below 750 K. Vacancy-mediated diffusion of Nb and Ta (which have similar average  $E_{KRAB}^m$ ) is expected to be reasonably facile above around 1000 K, while Mo and W are expected to be mobile only above 1500 K.

## Effect of Annealing Temperature on SRO

Figure 2a shows the first and second nearest neighbor (1NN and 2NN, respectively) SRO parameters obtained from structures annealed at different temperatures  $T_a$  from MC/MD simulations. It should be noted that these SRO values are based on full thermodynamic equilibrium and do not account for the kinetics discussed in the preceding section. We will discuss the combined effect of thermodynamics and kinetics in the next section.

Unsurprisingly, the magnitude of the observed SRO is the largest at low annealing temperatures (300 K) and gradually decreases with increase in the annealing temperature. Representative structures annealed at 300 K, 600 K, and 1200 K are shown in Figure 2b, c, and d, respectively. At an annealing temperature of 300 K, we observe a clear tendency to form alternating layers of elements of the same group, i.e., akin to the CsCl-type structure (Strukturbericht B2, Pearson type cP2) with one elemental group occupying the Cs site and the other elemental group occupying the Cl site. This is reflected in the positive (repulsive) 1NN SRO parameters between elements in the same group (W-Mo and Nb-Ta), and negative (attractive) 1NN SRO parameters between elements from different groups, as shown in Figure 2a. This

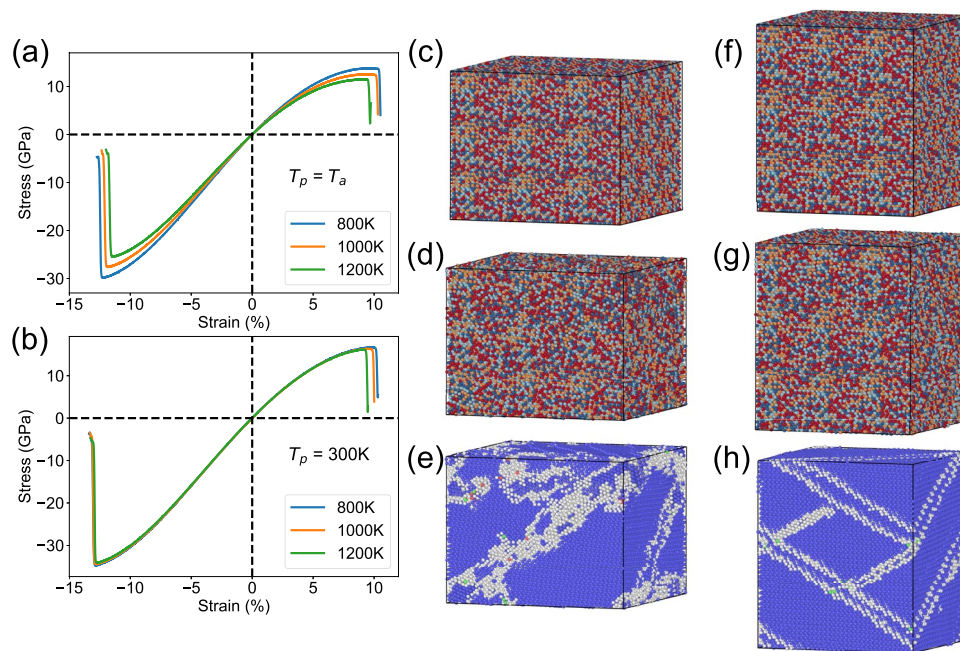


**Fig. 4** Uniaxial tensile/compressive tests of bulk MPEA structures annealed from 800 K, 1000 K, and 1200 K. **a** Uniaxial tensile/compressive tests are performed at the processing temperatures ( $T_p$ ), which is equal to  $T_a$ , as shown in the legend. **b** Tests are performed at room temperature (300 K). **c** and **f** are the structures ( $T_a = 800$  K and  $T_p = 300$  K) before the magnitude of stress drops dramatically; **d** and **g** are the snapshot of structures right after the stress drops. **e** and

**h** are the common neighbor analysis (CNA) for structures of **d** and **g**, respectively. Blue color regions characterize the BCC local structural environment, and gray color regions represent defects formed after plastic deformation. In Figure **h**, there are multiple  $\{112\}$  twinning planes slicing the bulk structure under tensile strain. The detailed characterizations of twins are presented in Figure 5. The ultimate tensile/compressive stress and corresponding strain are listed in Supplementary Information Table S1 (Color figure online)

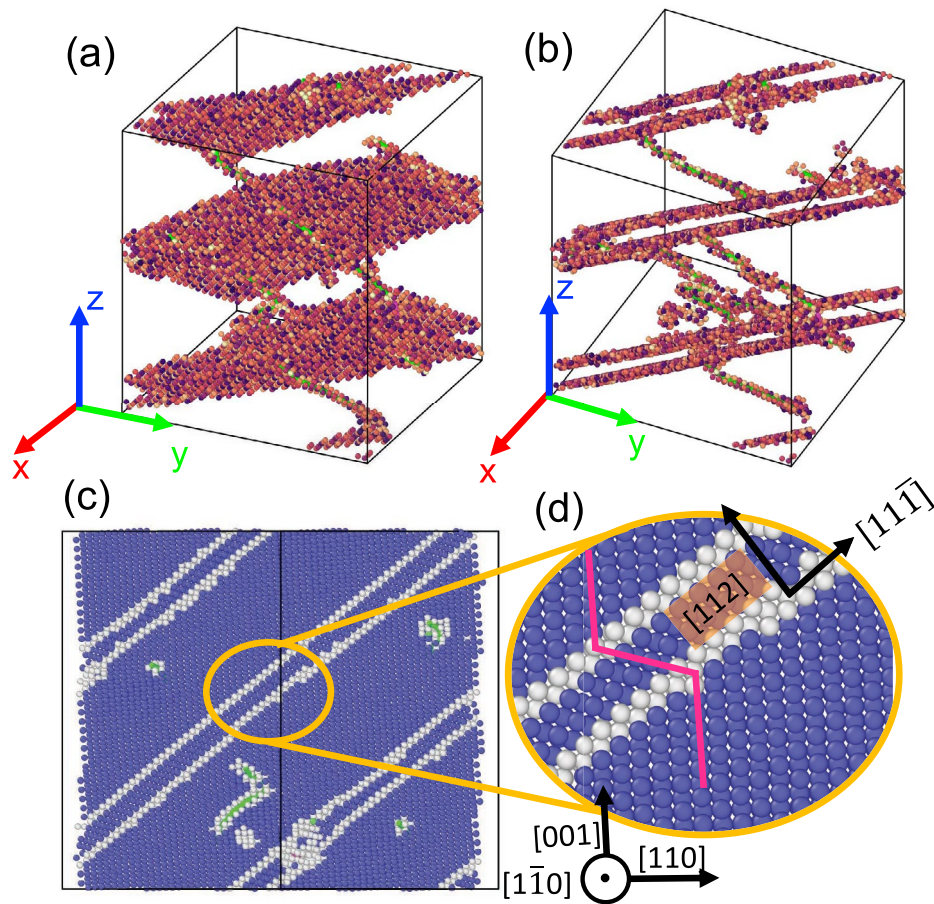


**Fig. 5** Twinning under uniaxial tension ( $T_p = 300$  K) of bulk MPEA structure annealed from 800K. The snapshot corresponds to strain = 11%. In **a** and **b**, atoms that are in a bcc-like local environment are removed to provide a clearer view of the twinning planes and dislocations. **a** shows that the twinning plane is  $\{112\}$  plane family, and **b** shows the thickness of the twinning boundary. Both views show the interactions between twinning planes and  $\frac{1}{2}\langle 111 \rangle$  screw dislocations. The atoms are colored by the per-atom potential energy. The bright green lines are  $\frac{1}{2}\langle 111 \rangle$  screw dislocations identified by the

Dislocation Extraction Algorithm (DXA) [44] algorithm. The bottom figures **c** and **d** are the cross-sectional view of the mirror-like twinning planes by slicing the bulk cell along  $\{1\bar{1}0\}$  plane as shown in the coordinate in the Figure. Similar to Figure 4c and d, atoms are colored by the CNA algorithm (blue = BCC, gray = defects/twins). From the zoom-in view of the twinning, we can observe the mirror images for the twin boundary as highlighted with the magenta segments. The twinning planes  $\{112\}$  are parallel to  $\langle 111 \rangle$  directions (Color figure online)

observation matches with the bonding preference reported by Widom et al. [37]. Conversely, the 2NN SRO parameters, which correspond to the distance between atoms in the same layer, have opposite signs from the corresponding 1NN SRO parameters for every pair of atoms. With increasing temperature, we observe increased disorder and disruption of the SRO. Structures annealed at 600K (Figure 2c) still clearly exhibit the characteristic B2 ordering, but structures annealed at 1200K (Figure 2d) have no discernible ordering and negligible SRO parameters.

### Effects of SRO on Stacking Fault Energy, Anti-phase Boundary Energy, and Critical Resolved Shear Stress Distribution

From the preceding sections, we may surmise that the eventual SRO observed in an MPEA is the result of competition between two effects. During initial synthesis at high temperatures, the NbTaMoW MPEA formed is likely to resemble a solid solution with little/no SRO. From Figure 1b, we may conclude that if the NbTaMoW MPEA was quenched and annealed at temperatures below 750 K, sluggish kinetics would likely result in negligible SRO formation. On the other hand, negligible SRO formation is also observed at temperatures above 1200K (Figure 2). Hence, appreciable

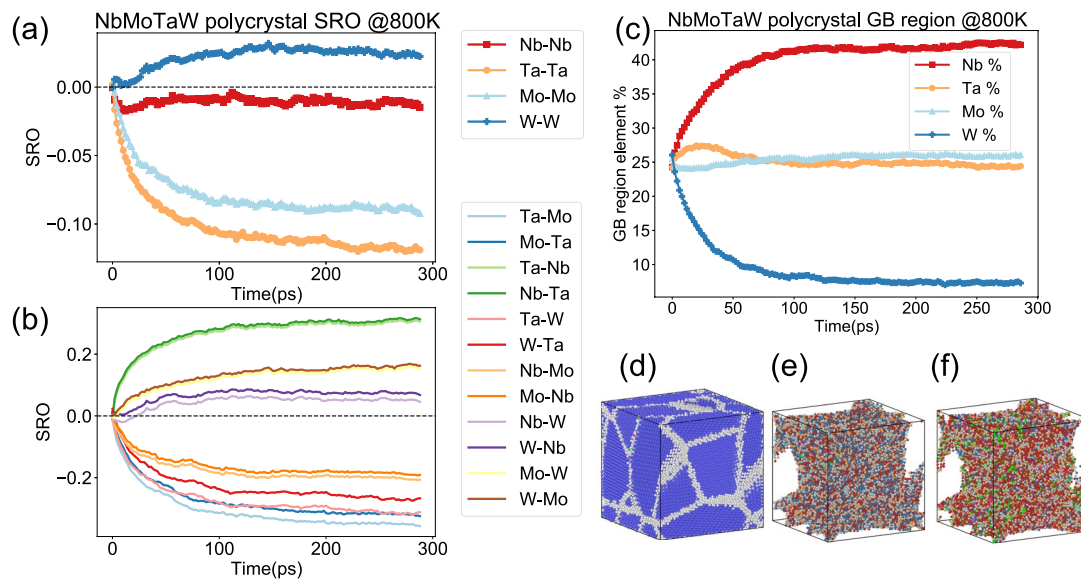


**Fig. 6** The SRO and segregation evolution of polycrystalline NbTaMoW MPEA in 800K MC/MD simulations. **a** and **b** show the SRO of the same element pairs and different element pairs, respectively. **c** shows the evolution of the element percentage in the grain boundary regions. The grain boundary region is the gray network, as shown in

**d**, colored using the CNA algorithm (blue=BCC, gray=grain boundary). **e** and **f** are the snapshots from the initial and final steps, where the BCC-like local environments were removed for ease of visualization. The bright green segments are  $1/2 \langle 111 \rangle$  screw dislocations identified by the DXA [44] algorithm (Color figure online)

SRO formation (within a reasonable amount of time) can form only via annealing within a temperature range between 800 K and 1200 K, primarily through the diffusion of Nb and Ta. In this section, we will explore the relationship between the degree of SRO and the stacking fault energy, anti-phase boundary energy, and critical resolved shear stress distribution within this temperature range.

Two of the most common slip systems for bcc-based alloys are  $\{110\} \langle 111 \rangle$  and  $\{112\} \langle 111 \rangle$  [23]. Figure 3 plots the distribution of the stacking fault energies (SFEs) and anti-phase boundary energies (APBEs) for the  $\{110\}$  and  $\{112\}$  planes of the NbTaMoW RMPEA annealed at different temperatures. There is an inverse relationship between the average SFE and APBE with the annealing temperature. The higher the annealing temperature, the lower the degree of SRO, the lower the average SFE and APBE. The mean values and standard deviations of SFE and APBE are annotated in Figure 3.

Such variations in the SFEs/APBEs will affect the migration of dislocations, the deformation mechanism, and the mechanical properties. It is known that  $1/2 \langle 111 \rangle$  screw dislocation plays an important role in the plasticity of bcc transition metals [38]. Recent experimental studies also revealed the dominant role of the screw dislocation in bcc refractory MPEAs [39, 40]. Figure 3e plots the distribution of the critical resolved shear stress (CRSS) of the screw dislocation with annealing temperature/chemical SRO. Starting from the bulk structures annealed at 800 K, 1000 K, and 1200 K,

a cylinder shape with one  $1/2 \langle 111 \rangle$  screw dislocation at the center along the  $z$  axis is created, as shown in Supplementary Information Figure S3. We sampled 100 dislocation local environments by positioning the center of the cylinder in a  $10 \times 10$  grid for each annealing temperature/SRO level. We applied a distance-dependent strain rate to enable the dislocation glide on 110 plane along the  $\langle 112 \rangle$  direction and recorded the stress when the dislocation started to move (i.e., CRSS) as shown in equation 2. The mean values of CRSS of  $1/2 \langle 111 \rangle$  screw dislocations are 1452, 1356, and 1271 MPa of structures annealed at 800 K, 1000 K, and 1200 K, respectively. Consistent with the SFE/APBEs, the lower the annealing temperature, the higher the stress needed for the migration of the screw dislocation. Comparing the  $T_a = 800$  K and 1200 K structures, the mean CRSS of the structure annealed at 800K is 14% higher than that annealed at 1200 K.

## Relationship Between Strength and Annealing Temperature

Figure 4 shows the results of uniaxial tensile/compressive tests of the NbTaMoW RMPEA annealed at different temperatures. The strain is applied along  $[001]$  direction at the processing temperatures ( $T_p$ ) that are equal to the annealing temperatures ( $T_a$ ) as shown in Figure 4a legend. Figure 4b shows the tensile tests performed at room temperature ( $T_p = 300$  K). The ultimate tensile/compressive strength and



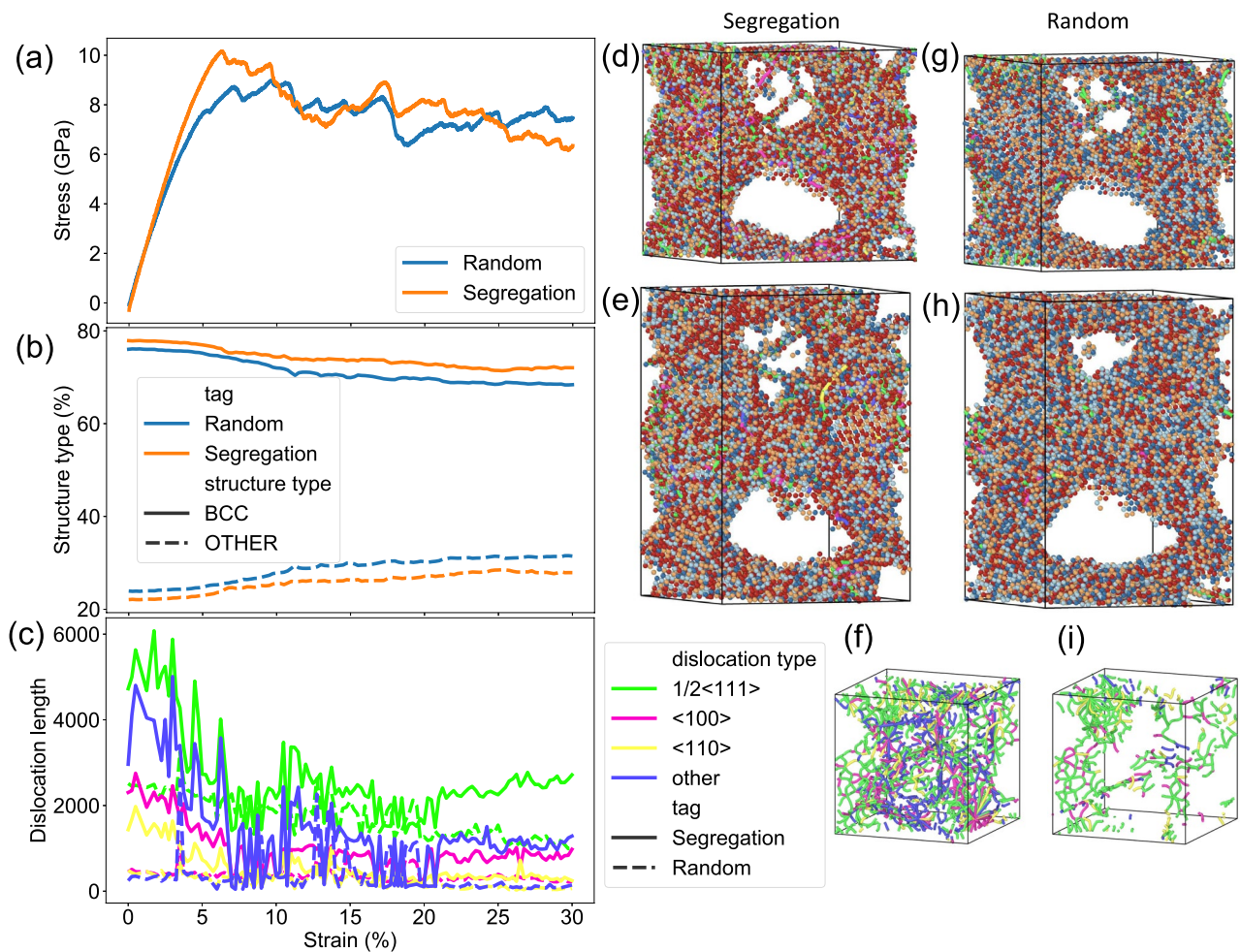


**Fig. 7** Uniaxial tensile tests at room temperature of polycrystal MPEA structures with/without Nb segregation. **a** Strain–stress curve of random solid solution and Nb-segregated NbTaMoW polycrystals. **b** and **c** plots showing the evolution of the fraction of structure types and dislocation lengths, respectively, with uniaxial tensile strain. **d** and **e** are the initial and final snapshots of polycrystals annealed from 800 K with Nb segregation. **g** and **h** are the initial and final snapshots of the polycrystals with random species distribution. The bcc-like

regions in all structure snapshots are removed for ease of visualization. A slab of thickness 60 Å along the (110) plane was created to characterize the grain boundary network. **f** and **i** are the dislocation network of the initial snapshot of polycrystals with/without segregation analyzed by (DXA) [44] algorithm. Different colors of line segments represent different types of dislocations, as shown in the legend of (c) (Color figure online)

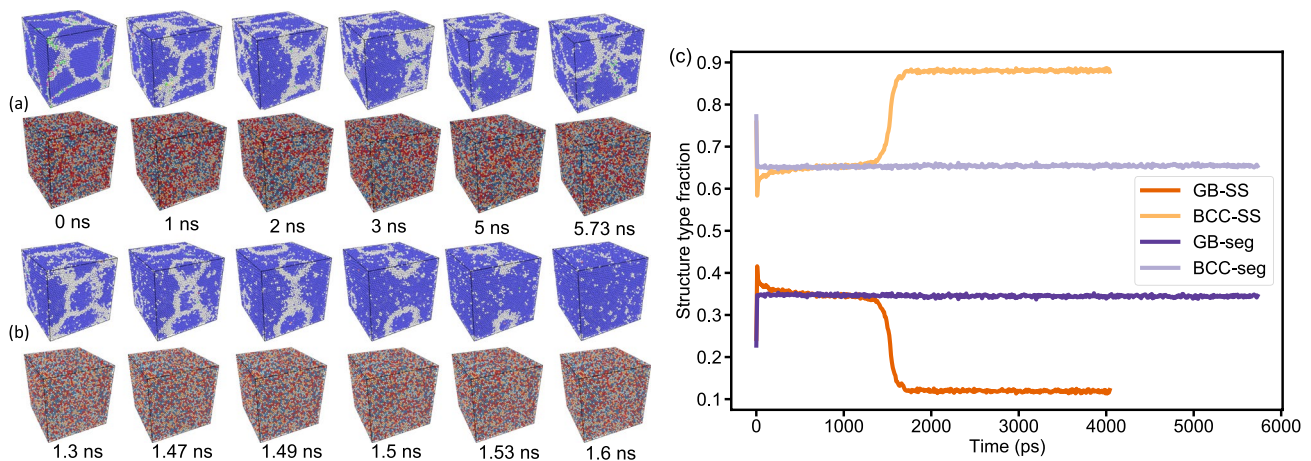
corresponding strain are listed in Supplementary Information Table S1. From Figure 4a and b, we may observe that the processing temperature has a significant effect on the strength of the RMPEA. In general, the tensile and compressive strengths decrease with increasing processing temperature. This is unsurprising given the increased mobility of atoms at higher temperatures and has been commonly observed for typical alloys. In contrast, the degree of SRO within the temperature range of 800–1200K has a relatively small effect on the strength of the NbTaMoW.

Figure 4c–e and f–h corresponds to the snapshots of structures ( $T_a=800$  K,  $T_p=300$  K) under compressive and tensile tests, respectively. Deformation twinning along {112} planes can be seen in the gray zone of Figure 4h. Figure 5

characterizes the twinning boundary planes and the interactions between twins and dislocation lines. Similar twins have been observed in the constituent bcc metals, i.e., Nb, Ta, Mo, and W, from both atomistic simulations and experiments [41–43].

### Effect of Annealing Temperature on Segregation and Polycrystal Properties

In practice, materials usually exist as polycrystals. To explore the effect of annealing temperature on segregation and SRO in polycrystalline NbTaMoW, we adopted the polycrystal structure from our previous work [8], which has an average grain diameter of about 7.5 nm. From Figure 6, it



**Fig. 8** The polycrystalline MPEA evolution under 2400 K MD simulation. **a** starts with the initial crystalline MPEA with Nb segregation, and SRO from 800 K MC/MD annealing, **b** starts with RSS polycrystalline MPEA. The first and third rows of atomic structures are colored according to the common neighbor analysis [48] OVITO [26] to distinguish the bcc regions (blue) and grain boundary regions (gray). In the second and forth rows of structures, atoms are colored

may be observed that polycrystals annealed at 800 K still exhibit the same Nb segregation observed in polycrystals annealed in our previous 300 K MC/MD simulations. The atomic % of Nb in GB regions equilibrates to around 40% (Figure 6c), far higher than the 25% expected for an equimolar RSS. Conversely, the atomic % of W decreases to around 10%. Similar to the previous work, it is observed that Nb segregation results in higher strength (Figure 7a).

This result can be explained by the evolution of defect percentage and dislocation length as shown in Figure 7b and c. Grain boundaries are barriers to dislocation motion. When a dislocation crosses a grain boundary, its direction of motion must change. There is a discontinuity of slip planes within the vicinity of a grain boundary. Compared to the RSS MPEA, the grain boundary is more stable in the Nb-segregated RMPEA. This is because Nb corresponds to the lowest GB energy compared to the rest of the constituent elements [45]. Therefore, extra stress/energy is needed for dislocations to move across the GB with a great % of Nb.

As reported by Yin et al. [11], cross-slip jogs are observed during screw dislocation glide. Additional stress must be applied for dislocations to break jogs. Comparing the polycrystals with and without Nb segregation, dislocations in the Nb-segregated NbTaMoW are constrained within the grain while those in the RSS NbTaMoW migrate and annihilate one another. The increase in the number/length of dislocations in Nb-segregated NbTaMoW polycrystals leads to more entanglements between dislocations. [46, 47]. Therefore, the dislocation lines become immobile due to the pinned jogs, leading to higher strength.

using the same code, as shown in Figure 2, where red, orange, light blue, and blue correspond to Nb, Ta, Mo, and W, respectively. **c** The polycrystalline MPEA structure evolution at 2400 K for both random solid solution structure (orange: GB and light orange: bcc bulk) and the structure with high SRO and Nb segregation (purple: GB and light purple: bcc bulk)

Figure 8 shows the evolution of the NbTaMoW polycrystals with and without Nb segregation in MD simulations at 2400 K. This temperature is selected as a representative operating temperature for such RMPEAs. It may be observed that Nb segregation has the effect of inhibiting initial grain growth, albeit within the short nanosecond time scale of the MD simulations. Figure 8c quantifies the changes in GB-like and bulk-like regions within the polycrystal. For the random solid solution NbTaMoW, the fraction of GB-like regions decreases from 35% to 10% with < 2 ns in the 2400 K MD simulations. These results suggest that segregation induced via annealing at intermediate temperatures can potentially be used to achieve microstructures that are more resistant to grain coarsening.

## Conclusion

To conclude, we have performed a comprehensive investigation of the effect of processing conditions on the NbTaMoWR MPEA using a highly accurate ML-IAP. These studies have shed important new insights into the relationship between the annealing temperature and mechanical properties such as the SFEs, APBEs, and CRSSs of the bulk NbMoTaW RMPEA. We have also further expanded our studies into the polycrystalline NbTaMoW RMPEA.

One important distinction between this work and previous studies using ML-IAPs is the consideration of diffusion kinetics during processing. Based on the predicted migration barriers and MC/MD simulations, it can be surmised that maximum SRO in NbTaMoW can be achieved

via multi-day annealing at an intermediate temperature of 800K–1000K. Lower temperatures would result in sluggish kinetics of elemental redistribution, while higher temperatures would result in a low equilibrium SRO. Higher SRO generally leads to higher SFEs, APBEs, and CRSSs, and hence, higher strength. Similar findings in fcc MPEAs have been reported [9, 30].

We further note that the previously observed Nb segregation to the GBs is still observed in polycrystalline NbTaMoW annealed at 800 K. Not only does this directly influence the SRO and mechanical properties, we also find that Nb segregation can potentially retard the grain growth of nanocrystalline NbTaMoW at high temperatures. Previous experimental reports have found that the yield strength of nanocrystalline NbTaMoW is one order of magnitude higher than the coarse-grained NbTaMoW and five times higher than the single crystal form [49]. Similarly, the chemically similar nanocrystalline VNbMoTaW has been reported to have extremely high hardness (11.4 GPa) compared to the coarse-grained alloy (5.25 GPa) [50]. The ultra-high hardness of nanocrystalline MPEA is mainly attributed to the Hall–Petch GB strengthening in addition to solid solution and dislocation hardening [50].

**Supplementary Information** The online version contains supplementary material available at <https://doi.org/10.1007/s44210-025-00065-3>.

**Acknowledgements** The authors acknowledge computational resources provided by the Triton Shared Computing Cluster (TSCC) at the University of California, San Diego.

**Funding** This research was supported by the National Science Foundation Materials Research Science and Engineering Center program through the UC Irvine Center for Complex and Active Materials (DMR-2011967). This work used Expanse at San Diego Supercomputer Center through allocation DMR150014 from the Advanced Cyberinfrastructure Coordination Ecosystem: Services & Support (ACCESS) program, which is supported by U.S. National Science Foundation grants #2138259, #2138286, #2138307, #2137603, and #2138296. The work also utilized software and data resources provided by the Materials Project, which is funded by the U.S. Department of Energy, Office of Science, Office of Basic Energy Sciences, Materials Sciences and Engineering Division under contract No. DE-AC02-05-CH11231 (Materials Project program KC23MP).

**Data Availability** The machine learning potential used to perform molecular dynamic simulations can be found at MAML GitHub repository [8]. For more details, visit the following link: [https://github.com/materialsvirtuallab/maml/tree/master/mvl\\_models/pes/MoNbTaW/snap.2020.06](https://github.com/materialsvirtuallab/maml/tree/master/mvl_models/pes/MoNbTaW/snap.2020.06).

## Declarations

**Conflict of interest** On behalf of all authors, the corresponding author states that there is no Conflict of interest.

**Open Access** This article is licensed under a Creative Commons Attribution 4.0 International License, which permits use, sharing, adaptation, distribution and reproduction in any medium or format, as long

as you give appropriate credit to the original author(s) and the source, provide a link to the Creative Commons licence, and indicate if changes were made. The images or other third party material in this article are included in the article's Creative Commons licence, unless indicated otherwise in a credit line to the material. If material is not included in the article's Creative Commons licence and your intended use is not permitted by statutory regulation or exceeds the permitted use, you will need to obtain permission directly from the copyright holder. To view a copy of this licence, visit <http://creativecommons.org/licenses/by/4.0/>.

## References

1. J.-W. Yeh, S.-K. Chen, S.-J. Lin, J.-Y. Gan, T.-S. Chin, T.-T. Shun, C.-H. Tsau, S.-Y. Chang, Nanostructured high-entropy alloys with multiple principal elements: novel alloy design concepts and outcomes. *Adv. Eng. Mater.* **6**, 299–303 (2004)
2. B. Cantor, I. Chang, P. Knight, A. Vincent, Microstructural development in equiatomic multicomponent alloys. *Mater. Sci. Eng., A* **375–377**, 213–218 (2004)
3. M.C. Gao, *High-Entropy Alloys* (New York, NY, Springer Science+Business Media, 2016)
4. R. Zhang, S. Zhao, J. Ding, Y. Chong, T. Jia, C. Ophus, M. Asta, R.O. Ritchie, A.M. Minor, Short-range order and its impact on the CrCoNi medium-entropy alloy. *Nature* **581**, 283–287 (2020)
5. F.X. Zhang, S. Zhao, K. Jin, H. Xue, G. Velisa, H. Bei, R. Huang, J. Ko, D.C. Pagan, J.C. Neufeld, W.J. Weber, Y. Zhang, Local structure and short-range order in a NiCoCr solid solution alloy. *Phys. Rev. Lett.* **118**, 205501 (2017)
6. X. Chen, Q. Wang, Z. Cheng, M. Zhu, H. Zhou, P. Jiang, L. Zhou, Q. Xue, F. Yuan, J. Zhu, X. Wu, E. Ma, Direct observation of chemical short-range order in a medium-entropy alloy. *Nature* **592**, 712–716 (2021)
7. S.D. Wang, X.J. Liu, Z.F. Lei, D.Y. Lin, F.G. Bian, C.M. Yang, M.Y. Jiao, Q. Du, H. Wang, Y. Wu, S.H. Jiang, Z.P. Lu, Chemical short-range ordering and its strengthening effect in refractory high-entropy alloys. *Phys. Rev. B* **103**, 104107 (2021)
8. X.-G. Li, C. Chen, H. Zheng, Y. Zuo, S.P. Ong, Complex strengthening mechanisms in the NbMoTaW multi-principal element alloy. *NPJ Comput. Mater.* **6**, 70 (2020)
9. J. Ding, Q. Yu, M. Asta, R.O. Ritchie, Tunable stacking fault energies by tailoring local chemical order in CrCoNi medium-entropy alloys. *Proc. Natl. Acad. Sci.* **115**, 8919–8924 (2018)
10. B. Yin, S. Yoshida, N. Tsuji, W.A. Curtin, Yield strength and misfit volumes of NiCoCr and implications for short-range-order. *Nat. Commun.* **11**, 2507 (2020)
11. S. Yin, Y. Zuo, A. Abu-Odeh, H. Zheng, X.-G. Li, J. Ding, S.P. Ong, M. Asta, R.O. Ritchie, Atomistic simulations of dislocation mobility in refractory high-entropy alloys and the effect of chemical short-range order. *Nat. Commun.* **12**, 4873 (2021)
12. Y. Zuo, C. Chen, X. Li, Z. Deng, Y. Chen, J. Behler, G. Csányi, A.V. Shapeev, A.P. Thompson, M.A. Wood, S.P. Ong, Performance and cost assessment of machine learning interatomic potentials. *J. Phys. Chem. A* **124**, 731–745 (2020)
13. H. Zheng, L. Fey, X.-G. Li, Y.-J. Hu, L. Qi, C. Chen, S. Xu, I.J. Beyerlein, S.P. Ong, Multi-scale investigation of short-range order and dislocation glide in MoNbTi and TaNbTi multi-principal element alloys. *NPJ Comput. Mater.* **9**, 89 (2023)
14. W. Ji, M.S. Wu, Retainable short-range order effects on the strength and toughness of NbMoTaW refractory high-entropy alloys. *Intermetallics* **150**, 107707 (2022)
15. Y. Cao, K. Sheriff, R. Freitas, Capturing Short-Range Order in High-Entropy Alloys with Machine Learning Potentials (2024)



16. A. Anand, C.V. Singh, Origin of gamma surface asymmetries in body-centered cubic refractory high entropy alloys. *Comput. Mater. Sci.* **233**, 112680 (2024)
17. Y. Pan, T. Fu, M. Duan, C. Li, H. Hu, X. Peng, Tension-compression asymmetry of BCC NbMoTaW in high entropy alloy nanowires. *ACS Appl. Nano Mater.* **7**, 8121–8129 (2024)
18. G. Kresse, J. Furthmüller, Efficient iterative schemes for Ab initio total-energy calculations using a plane-wave basis set. *Phys. Rev. B* **54**, 11169–11186 (1996)
19. P.E. Blöchl, Projector augmented-wave method. *Phys. Rev. B* **50**, 17953–17979 (1994)
20. J.P. Perdew, K. Burke, M. Ernzerhof, Generalized gradient approximation made simple. *Phys. Rev. Lett.* **77**, 3865–3868 (1996)
21. Z. Deng, Z. Zhu, I.-H. Chu, S.P. Ong, Data-driven first-principles methods for the study and design of alkali superionic conductors. *Chem. Mater.* **29**, 281–288 (2017)
22. S.P. Ong, W.D. Richards, A. Jain, G. Hautier, M. Kocher, S. Cholia, D. Gunter, V.L. Chevrier, K.A. Persson, G. Ceder, Python materials genomics (pymatgen): a robust, open-source python library for materials analysis. *Comput. Mater. Sci.* **68**, 314–319 (2013)
23. W. Callister Jr, D.G. Rethwisch, *Materials Science and Engineering: An Introduction* (Wiley, Hoboken, 2013)
24. G. Neumann, C. Tuijn, Self-diffusion and impurity diffusion in pure metals: handbook of experimental data, 1st ed.; Pergamon materials series 14; Pergamon: Amsterdam ; Boston ; London, (2009); OCLC: ocn229026068
25. S. Plimpton, Fast parallel algorithms for short-range molecular dynamics. *J. Comput. Phys.* **117**, 1–19 (1995)
26. A. Stukowski, Visualization and analysis of atomistic simulation data with OVITO—the open visualization tool. *Modell. Simul. Mater. Sci. Eng.* **18**, 015012 (2010)
27. V.V. Bulatov, W. Cai, *Computer Simulations of Dislocations; Oxford Series on Materials Modelling 3* (Oxford University Press, Oxford, 2006)
28. F. Maresca, D. Dragoni, G. Csányi, N. Marzari, W.A. Curtin, Screw dislocation structure and mobility in body centered cubic Fe predicted by a Gaussian approximation potential. *NPJ Comput. Mater.* **4**, 69 (2018)
29. H. Föll, Defects in Crystals. [https://www.tf.uni-kiel.de/matwis/amat/def\\_en/](https://www.tf.uni-kiel.de/matwis/amat/def_en/), (Accessed: 2024-05-19)
30. Q.-J. Li, H. Sheng, E. Ma, Strengthening in multi-principal element alloys with local-chemical-order roughened dislocation pathways. *Nat. Commun.* **10**, 3563 (2019)
31. A. Van der Ven, G. Ceder, M. Asta, P.D. Tapesch, First-principles theory of ionic diffusion with nondilute carriers. *Phys. Rev. B* **64**, 184307 (2001)
32. O. Senkov, G. Wilks, D. Miracle, C. Chuang, P. Liaw, Refractory high-entropy alloys. *Intermetallics* **18**, 1758–1765 (2010)
33. Y. Zou, S. Maiti, W. Steurer, R. Spolenak, Size-dependent plasticity in an Nb<sub>25</sub>Mo<sub>25</sub>Ta<sub>25</sub>W<sub>25</sub> refractory high-entropy alloy. *Acta Mater.* **65**, 85–97 (2014)
34. Y.A. Kraftmakher, Vacancy formation in niobium. *Soviet Phys.-Solid State (English Transl.)* **1963**(5)
35. Y. Tang, L. Zhang, Effect of thermal vacancy on thermodynamic behaviors in BCC W close to melting point: a thermodynamic study. *Materials* **11**, 1648 (2018)
36. P.-W. Ma, S.L. Dudarev, Effect of stress on vacancy formation and migration in body-centered-cubic metals. *Phys. Rev. Mater.* **3**, 063601 (2019)
37. M. Widom, W.P. Huhn, S. Maiti, W. Steurer, Hybrid Monte Carlo/ molecular dynamics simulation of a refractory metal high entropy alloy. *Metall. Mater. Trans. A* **45**, 196–200 (2014)
38. J.W. Christian, Some surprising features of the plastic deformation of body-centered cubic metals and alloys. *Metall. Trans. A* **14**, 1237–1256 (1983)
39. L. Lilensten, J.-P. Couzinié, L. Perrière, A. Hocini, C. Keller, G. Dirras, I. Guillot, Study of a Bcc multi-principal element alloy: tensile and simple shear properties and underlying deformation mechanisms. *Acta Mater.* **142**, 131–141 (2018)
40. G. Dirras, J. Gubicza, A. Heczal, L. Lilensten, J.-P. Couzinié, L. Perrière, I. Guillot, A. Hocini, Microstructural investigation of plastically deformed Ti<sub>20</sub>Zr<sub>20</sub>Hf<sub>20</sub>Nb<sub>20</sub>Ta<sub>20</sub> high entropy alloy by X-Ray diffraction and transmission electron microscopy. *Mater. Charact.* **108**, 1–7 (2015)
41. S. Mahajan, D.F. Williams, Deformation twinning in metals and alloys. *Int. Metall. Rev.* **18**, 43–61 (1973)
42. J. Wang, Z. Zeng, M. Wen, Q. Wang, D. Chen, Y. Zhang, P. Wang, H. Wang, Z. Zhang, S.X. Mao, T. Zhu, Anti-twinning in nanoscale tungsten. *Sci. Adv.* **6**, eaay2792 (2020)
43. R. Gröger, J. Holzer, T. Kruml, Twinning and antitwinning in body-centered cubic metals. *Comput. Mater. Sci.* **216**, 111874 (2023)
44. A. Stukowski, V.V. Bulatov, A. Arsenlis, Automated identification and indexing of dislocations in crystal interfaces. *Modell. Simul. Mater. Sci. Eng.* **20**, 085007 (2012)
45. H. Zheng, X.-G. Li, R. Tran, C. Chen, M. Horton, D. Winston, K.A. Persson, S.P. Ong, Grain boundary properties of elemental metals. *Acta Mater.* **186**, 40–49 (2020)
46. D. Roylance, The dislocation basis of yield and creep - web.mit.edu. <https://web.mit.edu/course/3/3.11/www/modules/dn.pdf>
47. G. Dieter, D. Bacon, D. Bacon, Mechanical metallurgy. *Materials Science and Engineering Series* (McGraw-Hill, New York, 1988)
48. A. Stukowski, Structure identification methods for atomistic simulations of crystalline materials. *Modell. Simul. Mater. Sci. Eng.* **20**, 045021 (2012)
49. Y. Zou, J.M. Wheeler, H. Ma, P. Okle, R. Spolenak, Nanocrystalline high-entropy alloys: a new paradigm in high-temperature strength and stability. *Nano Lett.* **17**, 1569–1574 (2017)
50. S. Xin, M. Zhang, T. Yang, Y. Zhao, B. Sun, T. Shen, Ultrahard bulk nanocrystalline VNbMoTaW high-entropy alloy. *J. Alloy. Compd.* **769**, 597–604 (2018)

**Publisher's Note** Springer Nature remains neutral with regard to jurisdictional claims in published maps and institutional affiliations.